

## Article

# Integral Sliding Mode Control for Maximum Power Point Tracking in DFIG Based Floating Offshore Wind Turbine and Power to Gas

Lin Pan <sup>1,2,3,4</sup> , Ze Zhu <sup>1,\*</sup> , Yong Xiong <sup>5,†</sup>  and Jingkai Shao <sup>6,†</sup> 

<sup>1</sup> School of Logistics Engineering, Wuhan University of Technology, Wuhan 430063, China; lin.pan@whut.edu.cn

<sup>2</sup> Shaoxing Institute of Advanced Research, Wuhan University of Technology, Shaoxing 312300, China

<sup>3</sup> Zhongshan Institute of Advanced Engineering Technology of WUT, Zhongshan 528437, China

<sup>4</sup> Key Laboratory of Marine Power Engineering and Technology (Ministry of Transport), Wuhan University of Technology, Wuhan 430063, China

<sup>5</sup> School of Navigation, Wuhan University of Technology, Wuhan 430063, China; xiong@whut.edu.cn

<sup>6</sup> Guangxi LiuGong Machinery Co., Ltd., Liuzhou 545007, China; jingkaishao@hotmail.com

\* Correspondence: zhuze1202@whut.edu.cn

† These authors contributed equally to this work.

**Abstract:** This paper proposes a current decoupling controller for a Doubly-fed Induction Generator (DFIG) based on floating offshore wind turbine and power to gas. The proposed controller realizes Maximum Power Point Tracking (MPPT) through integral sliding mode compensation. By using the internal model control strategy, an open-loop controller is designed to ensure that the system has good dynamic performance. Furthermore, using the integral Sliding Mode Control (SMC) strategy, a compensator is designed to eliminate the parameter perturbation and external disturbance of the open-loop control. The parameters of the designed controller are designed through Grey Wolf Optimization (GWO). Simulation results show that the proposed control strategy has better response speed and smaller steady-state error than the traditional control strategy. This research is expected to be applied to the field of hydrogen production by floating offshore wind power.

**Keywords:** floating offshore wind turbine; doubly-fed induction generator (DFIG); integral sliding mode control (ISMC); maximum power point tracking (MPPT); power to gas



**Citation:** Pan, L.; Zhu, Z.; Xiong, Y.; Shao, J. Integral Sliding Mode Control for Maximum Power Point Tracking in DFIG Based Floating Offshore Wind Turbine and Power to Gas.

*Processes* **2021**, *9*, 1016. <https://doi.org/10.3390/pr9061016>

Academic Editor: Krzysztof Rogowski

Received: 13 May 2021

Accepted: 4 June 2021

Published: 9 June 2021

**Publisher's Note:** MDPI stays neutral with regard to jurisdictional claims in published maps and institutional affiliations.



**Copyright:** © 2021 by the authors. Licensee MDPI, Basel, Switzerland. This article is an open access article distributed under the terms and conditions of the Creative Commons Attribution (CC BY) license (<https://creativecommons.org/licenses/by/4.0/>).

## 1. Introduction

Since the industrial revolution, energy has become the fundamental power for human production and development. On the one hand, natural reserves of non-renewable resources such as oil and coal are limited. After being consumed by humans for centuries, such resources are gradually depleted. On the other hand, after the combustion of various fossil fuels, a large amount of toxic gas (including nitrogen oxides and sulfur oxides) and particulate matter will be emitted, which will increase the risk of respiratory diseases [1]. Under such circumstances, various renewable energy utilization schemes such as wind energy and solar energy have been proposed [2]. Due to its unique advantages, Doubly-fed Induction Generators (DFIG) occupy a large proportion in the field of wind power generation. The performance of the drive control system is directly related to the operating performance of the generator [3]. Therefore, the generator control strategy is the key to affecting generator performance.

Including doubly-fed induction generators, the induction motors are multi-variable and strongly coupled systems. The vector control is the strategy, which transforms the three-phase asynchronous motor system into the DC motor system through coordinate transformation, thereby achieving independent control of torque and flux components [4]. The vector control will overlap the coordinate system with a certain vector of the motor.

They are the available vectors, such as stator flux, stator voltage, air gap flux, rotor flux, etc. [5]. Generally, a DFIG wind power system using vector control is designed as a double closed loop structure. The two PI controllers are used to control the speed and reactive power separately in the outer loop. At the same time, the two PI controllers are used to control the  $d$ -axis current component and the  $q$ -axis current component, respectively, in the inner loop [6]. In [7], the author proposed a robust proportional-integral (PI) controller with its parameters designed by constrained population extremal optimization for the load frequency control problem. Zeng proposed a hybrid method combined adaptive control, neural network, and PID and proved its effectiveness for a nonlinear system in [8]. For this control structure, some studies have adjusted the parameters of the PI controller by applying a heuristic algorithm to obtain better power capture performance [9,10]. Qi investigated the event-triggered  $L_\infty$  control for network-based switched linear systems with transmission delay in [11] and proposed  $H_\infty$  filtering for networked switched systems in [12].

With the development of floating offshore wind turbines over the world, their reliability and dynamic performance requirements have gradually increased [13,14]. Although vector control theory can be used to convert a doubly-fed floating offshore wind turbine system into a linear system. However, in fact, the doubly-fed wind turbine system is still nonlinear, and it often contains a large amount of time delay and coupling components in the actual working environment [15–17]. With the increase of coupling effect, its torque may produce transient distortion, which affects the dynamic performance of the system, and then causes the maximum power point to not coincide with the actual working state [18]. Therefore, it has been difficult for the simple PI control system to meet the increasingly high work requirements, and more advanced controllers need to be designed according to modern control technology. It is worth mentioning that floating offshore wind energy develops rapidly in developing countries in recent years, such as China.

Floating offshore wind power generation technology provides new ideas for solving the problem of wind curtailment. It is of great significance for solving the problem of floating offshore wind power consumption, and development of decentralized wind power generation technology, realizing multi-channel and efficient use of renewable energy [19]. Wind power generation hydrogen is the method by using electrolysis of water energy storage. On the one hand, it can integrate hydrogen as a clean and high-energy fuel into the existing gas supply network and realize the complementary conversion of electricity to gas. On the other hand, it can directly use hydrogen energy in high-efficiency and clean technologies such as fuel cells. For example, Figure 1 shows the description of floating offshore wind turbines and power to gas [20]. Usually, the floating offshore wind turbines are located in the deep sea and have the advantages of abundant wind resources.

Sliding mode control is a nonlinear control method, which is characterized by discontinuous control. It can make the system switch from one continuous structure to another continuous structure in the state space, so this is a variable structure control method. The control design of sliding mode control will change the dynamic characteristics of the system so that the state trajectory moves along the boundary of the control structure. This boundary is called the sliding surface. The sliding surface can be designed as required, and the movement of the system trajectory on the sliding surface is not affected by the parameters of the controlled object and external interference. Therefore, sliding mode control has the advantages of fast response and insensitivity to external interference [21].

In recent years, with the development of computer technology and high-power electronic switching elements, the realization of sliding mode control has become easier. For such complex nonlinear systems as wind power systems, it is suitable to use sliding mode control theory to design controllers that meet performance requirements. It can improve the dynamic performance of wind turbines by using the sliding mode controller instead of the PI controller for speed control [22,23]. In Ref. [24], SMC is used for direct power control of a doubly-fed induction generator wind turbine operating in unbalanced grid voltage conditions. In Ref. [25], an improved strategy of SMC is used for the controller design of

a variable speed wind turbine with a fractional order doubly fed induction generator. In Ref. [26], a combination of sliding mode control and phase-locked loop estimator is used for the sensorless vector control strategy of a rotor-tied doubly fed induction generator system. In Ref. [27], an adaptive gain second-order sliding mode direct power control strategy is proposed, which can work normally in a DFIG wind turbine system with unbalanced grid voltage.

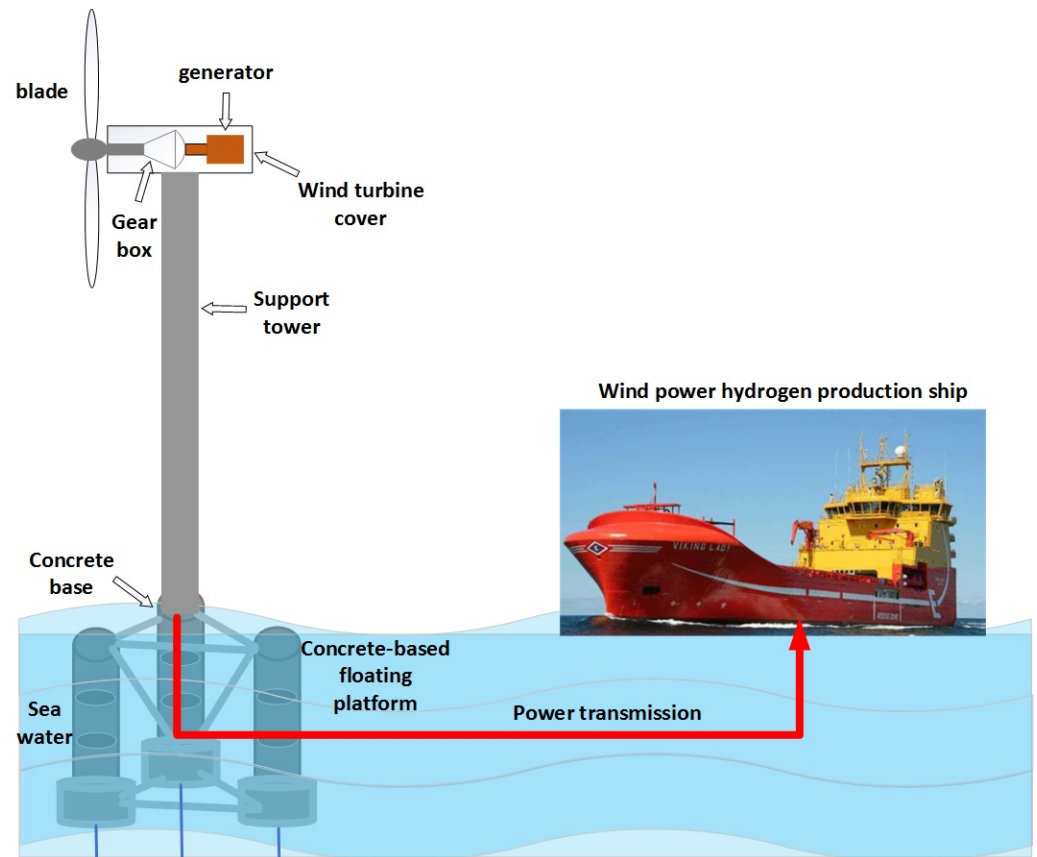


**Figure 1.** The description of floating offshore wind turbines and power to gas.

In view of the rich characteristics of floating offshore wind energy resources, this study focuses on high-power floating offshore wind power generation systems. Based on the above studies, in order to solve the problem of insufficient dynamic performance and robustness of traditional dual closed-loop PI controllers, this paper proposes a new MPPT control strategy. According to the principle of internal model control, an internal model open-loop controller is designed. In addition, in order to improve the controller's ability to resist external disturbances, the sliding mode theory is used to compensate the errors of the internal-mode open-loop controller. The novelty of this study is the use of a new sliding mode controller structure. In the proposed control method, a sliding mode controller is used to compensate the output error instead of directly outputting the control signal. This is different from most DFIG wind turbine systems based on sliding mode control. In order to verify the accuracy and reliability of the proposed controller, the proposed controller was simulated and verified in Matlab software.

The structure of the article is as follows: Section 2 describes the DFIG floating offshore wind turbine system model. Section 3 introduces the design of the proposed controller and gives a detailed proof of system stability. In Section 4, the proposed control method is simulated, and the simulation results are analyzed. Finally, it is summarized in Section 5.

## 2. DFIG Floating Offshore Wind Turbine System Modeling

The doubly-fed floating offshore wind turbine system is shown in Figure 2. The generator used in this power generation system is a Doubly-Fed Induction Generator [28]. The floating offshore wind turbine is connected to the generator rotor through a gearbox. At the same time, the rotor is excited by a power converter, and the generator stator is connected to the grid. A variable-speed constant-frequency power generation system using a doubly-fed floating offshore wind turbine is one of the popular forms of current wind energy conversion systems. Decoupling control of active and reactive power in floating offshore wind turbine systems can be achieved by applying dual PWM converters. This kind of wind energy conversion system has the regulation capability similar to that of a synchronous motor, and can regulate the voltage and frequency of the power grid. In addition, the power converter is located on the rotor side, and the power of the rotor side circuit depends on the generator slip power. Therefore, its actual power is only about 30% of the generator capacity, which greatly reduces the size and cost of the power converter. Due to such advantages of the doubly-fed floating offshore wind turbine system, the industry has conducted in-depth research on the converter control strategy of this system.

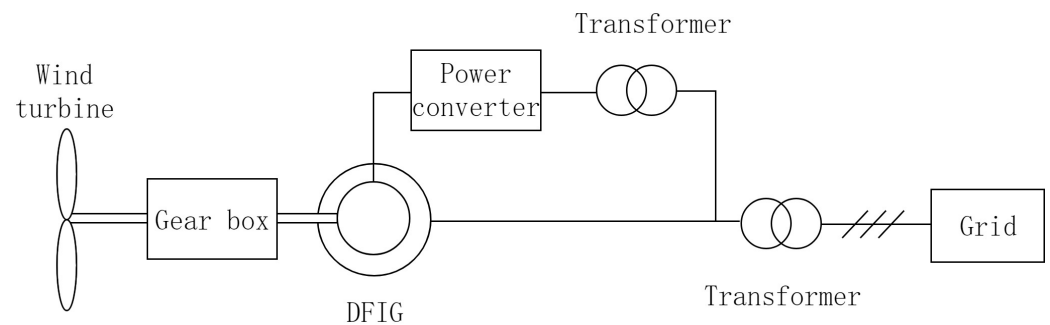


**Figure 2.** Description of the DFIG wind power system.

### 2.1. Floating Offshore Wind Turbine Model

In the doubly-fed floating offshore wind turbine system, the floating offshore wind turbine is used to convert wind energy into mechanical energy, and the generator is used to convert mechanical energy into electrical energy. The mechanical energy is transmitted between the floating offshore wind turbine and the generator through a transmission structure such as a transmission shaft and a gearbox. The total amount of mechanical energy output by a floating offshore wind turbine is mainly determined by the wind speed and the aerodynamic characteristics of the floating offshore wind turbine. At the same time, the mechanical energy characteristics delivered to the generator are also closely related to the mechanical characteristics of the transmission system. The wind energy captured by an floating offshore wind turbine is usually described by Equation (1) [29]:

$$P_m = 0.5C_p(\lambda, \beta)\rho Av^3 \quad (1)$$

where  $P_m$  is the output power of the floating offshore wind turbine,  $C_p$  is the power coefficient, and it is related to the tip speed ratio  $\lambda$  and pitch angle  $\beta$ ,  $\rho$  is the air density,  $A$  is the area swept by the pales of the turbine, and  $v$  is the wind speed.

The power coefficient can be written as Equation (2) [30]:

$$\begin{cases} C_p(\lambda, \beta) = c_1 \left( \frac{c_2}{\lambda_i} - c_3\beta - c_4 \right) e^{-\frac{c_5}{\lambda_i}} + c_6\lambda \\ \frac{1}{\lambda_i} = \frac{1}{\lambda + 0.08\beta} - \frac{0.035}{\beta^3 + 1} \end{cases} \quad (2)$$

The definition of tip-speed-ratio  $\lambda$  is as the follows. The ratio of the linear velocity of the floating offshore wind turbine blade tip to the wind speed is  $\lambda$ , that is,  $\lambda = \omega R/v$ ,

$\omega$  is the angular speed of the floating offshore wind turbine,  $R$  is the blade length, and  $c_i (i = 1, 2, 3, 4, 5, 6)$  are constants related to the characteristics of the floating offshore wind turbine. The parameters used in this study are  $c_1 = 0.22$ ,  $c_2 = 116$ ,  $c_3 = 0.4$ ,  $c_4 = 5$ ,  $c_5 = 12.5$ , and  $c_6 = 0$ .

The relationship between power coefficient, tip speed ratio, and pitch angle is shown in Figure 3.

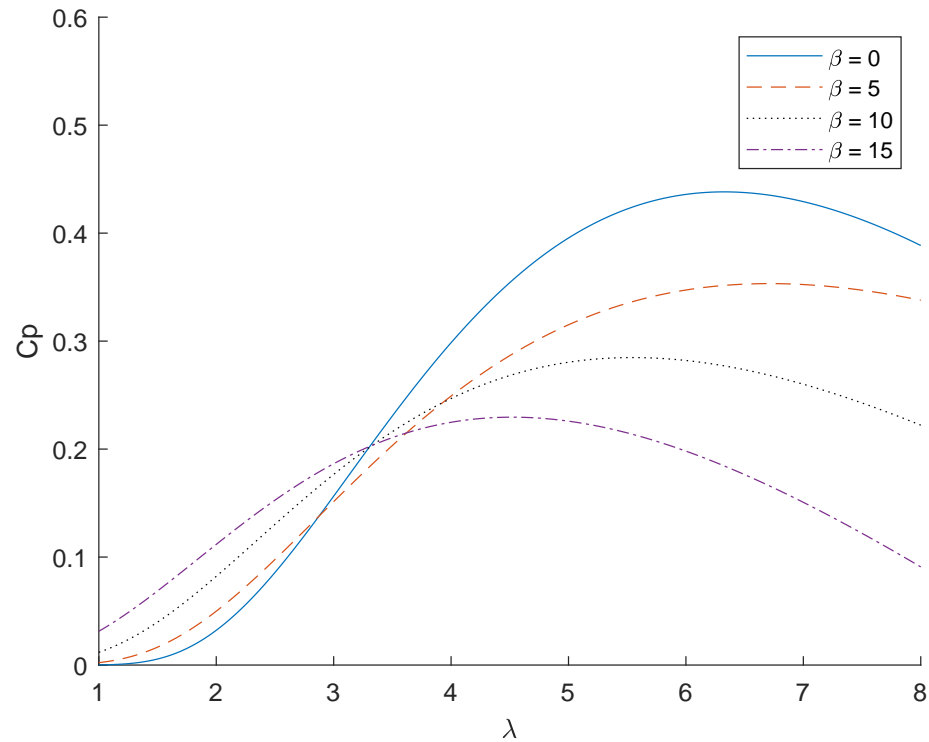


Figure 3. Aerodynamic characteristics of floating offshore wind turbines.

It can be known from the above analysis that there is an optimal tip speed ratio  $\lambda_{opt}$ , which makes the captured wind energy the largest by the floating offshore wind turbine at this tip speed ratio. Therefore, the reference value of the rotational speed of the floating offshore wind turbine can be given by Equation (3):

$$\omega_r^* = \lambda_{opt} v / R \quad (3)$$

## 2.2. DFIG Model

The mathematical model of an induction motor has the characteristics of multi-variable, strong coupling, nonlinearity, and time-varying. It is very inconvenient to analyze it. The original model can be transformed by vector control theory to obtain the state equation of DFIG in the synchronous rotating coordinate system [28]. Its dynamic characteristics can be described by Equations (4) and (5):

$$\begin{bmatrix} u_{sd} \\ u_{sq} \\ u_{rd} \\ u_{rq} \end{bmatrix} = \begin{bmatrix} R_s & 0 & 0 & 0 \\ 0 & R_s & 0 & 0 \\ 0 & 0 & R_r & 0 \\ 0 & 0 & 0 & R_r \end{bmatrix} \begin{bmatrix} i_{sd} \\ i_{sq} \\ i_{rd} \\ i_{rq} \end{bmatrix} + \begin{bmatrix} p & -\omega_1 & 0 & 0 \\ \omega_1 & p & 0 & 0 \\ 0 & 0 & p & \omega_r - \omega_1 \\ 0 & 0 & \omega_1 - \omega_r & p \end{bmatrix} \begin{bmatrix} \psi_{sd} \\ \psi_{sq} \\ \psi_{rd} \\ \psi_{rq} \end{bmatrix} \quad (4)$$

$$T_e = \frac{3}{2}n_p(\psi_{sd}i_{sq} - \psi_{sq}i_{sd}) = T_L + \frac{J}{n_p} \frac{d\omega_r}{dt} + \frac{D}{n_p}\omega_r \quad (5)$$

where  $u_{sd}$  and  $u_{sq}$  are voltage components of the stator in  $d$ -axis and  $q$ -axis,  $u_{rd}$  and  $u_{rq}$  are voltage components of the rotor in  $d$ -axis and  $q$ -axis,  $i_{sd}$  and  $i_{sq}$  are current components of the stator in  $d$ -axis and  $q$ -axis,  $i_{rd}$  and  $i_{rq}$  are current components of the rotor in  $d$ -axis and  $q$ -axis,  $R_s$  and  $R_r$  are the resistances of the stator and rotor,  $\psi_{sd}$  and  $\psi_{sq}$  are the flux components of the stator in  $d$ -axis and  $q$ -axis, and  $\psi_{rd}$  and  $\psi_{rq}$  are the flux components of the rotor in  $d$ -axis and  $q$ -axis.  $\omega_1$  is the synchronous electromagnetic angular velocity,  $\omega_r$  is the rotor electromagnetic angular velocity,  $p$  is the differential operator,  $T_e$  is the electromagnetic torque,  $n_p$  is the number of pole pairs,  $T_L$  is the external load,  $J$  is the moment of inertia, and  $D$  is the damping coefficient.

The relationship between flux and current is shown in Equation (6):

$$\begin{bmatrix} \psi_{sd} \\ \psi_{sq} \\ \psi_{rd} \\ \psi_{rq} \end{bmatrix} = \begin{bmatrix} L_s & 0 & L_m & 0 \\ 0 & L_s & 0 & L_m \\ L_m & 0 & L_r & 0 \\ 0 & L_m & 0 & L_r \end{bmatrix} \begin{bmatrix} i_{sd} \\ i_{sq} \\ i_{rd} \\ i_{rq} \end{bmatrix} \quad (6)$$

where  $L_s$  is the stator inductance,  $L_r$  is the rotor inductance, and  $L_m$  is the mutual inductance.

In stator flux orientation vector control, the direction of the stator flux is coincident with the  $d$ -axis of the synchronous rotation coordinate system. Assuming that the DFIG winding is directly connected to an infinitely large power grid, parameters such as the voltage amplitude, phase, and angular frequency of the grid can be considered as the constant, and the stator flux can be regarded as a fixed value. If the stator resistance is ignored,  $\psi_{sd} = \psi_s$  and  $\psi_{sq} = 0$ . One has the following results in Equations (7) and (8):

$$\begin{cases} u_{sd} = p\psi_s = 0 \\ u_{sq} = \omega_1\psi_s = u_s \end{cases} \quad (7)$$

$$\begin{cases} i_{sd} = \frac{\psi_s}{L_s} - \frac{i_{rd}L_m}{L_s} \\ i_{sq} = -\frac{i_{rq}L_m}{L_s} \end{cases} \quad (8)$$

Substituting Equations (7) and (8) into (4), we know that

$$\begin{cases} \frac{di_{rd}}{dt} = -\frac{R_r}{\sigma L_r}i_{rd} + (\omega_1 - \omega_r)i_{rq} + \frac{1}{\sigma L_r}u_{rd} \\ \frac{di_{rq}}{dt} = -\frac{R_r}{\sigma L_r}i_{rq} - (\omega_1 - \omega_r)\left(\frac{L_m}{\sigma L_s L_r}\psi_s + i_{rd}\right) + \frac{1}{\sigma L_r}u_{rq} \end{cases} \quad (9)$$

where  $\sigma$  is the leakage coefficient, and its definition is shown in Equation (10):

$$\sigma = 1 - \frac{L_m^2}{L_s L_r} \quad (10)$$

It can be known from the above analysis that the decoupling of active power and reactive power of the stator has been realized by vector control. Generator stator active power can be controlled by the rotor current  $q$ -axis component, and stator reactive power can be controlled by the rotor current  $d$ -axis component. Considering that the rotor voltage balance is not completely decoupled, the feedforward term is defined as shown in Equation (11):

$$\begin{cases} u_{rd}' = (\omega_1 - \omega_r)\sigma L_r i_{rq} \\ u_{rq}' = -(\omega_1 - \omega_r)\left(\frac{L_m}{L_s}\psi_s + \sigma L_r i_{rd}\right) \end{cases} \quad (11)$$



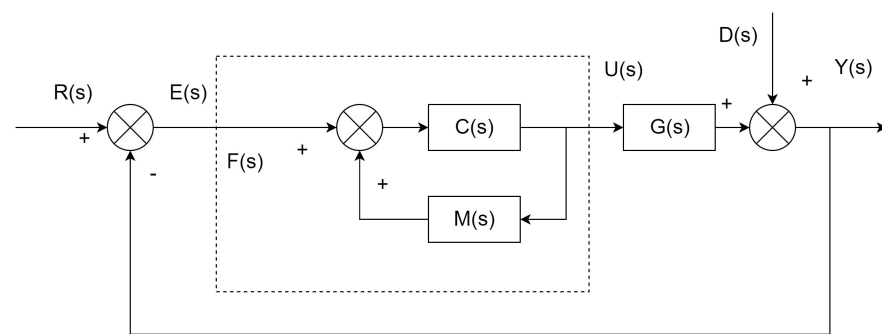


**Figure 5.** Description of internal model control.

According to Figure 5, the system input–output transfer function is shown in Equation (13).

$$Y(s) = \frac{C(s)G(s)}{1 + Cs[Gs - Ms]}R(s) + \frac{1 - C(s)G(s)}{1 + Cs[Gs - Ms]}D(s) \quad (13)$$

It is assumed that the internal model can be fully described by the system model, that is,  $M(s) = G(s)$ . When  $C(s) = M^{-1}(s)$ , there is  $Y(s) = R(s)$ . In this ideal state, it is not necessary to adjust any control parameters to make the output of the system fully track the reference input. In addition, since the system output does not include interference signal components, the controller can be considered to be able to overcome any interference signals.

However, in an actual system, the above ideal controller is difficult to implement for the following reasons:

- (i) When the controlled system  $G(s)$  contains time-delay components, the controller  $C(s)$  will contain lead components, which does not conform to physical reality and is difficult to achieve;
- (ii) When the right half-plane zeros exist in the controlled system  $G(s)$ , the controller  $C(s)$  will contain the right half-plane poles, and the controller will be unstable at this time, which will affect the stability of the entire system;
- (iii) When the order of the denominator polynomial in the controlled system  $G(s)$  is higher than the numerator, the controller  $C(s)$  will include a differentiator. Since the differentiator is extremely sensitive to signal noise, it is not suitable for practical use;
- (iv) When there is a model error, that is,  $M(s) \neq G(s)$ , the ideal controller will not guarantee the stability of the system.

Due to the above reasons, there are two steps in the designing of the controller. First, the controlled system  $G(s)$  is been decomposed. The smallest phase part has been found that does not include the time delay components and the zero point in the right half plane. The minimum phase part is the internal mode  $M(s)$  of the control system. Then, the controller is constructed by inverting the internal model and adding a filter, which is shown in Equation (14):

$$C(s) = \frac{L(s)}{M(s)} \quad (14)$$

where  $L(s)$  is a low-pass filter, as shown in Equation (15):

$$L(s) = \frac{\alpha}{(s + \alpha)} \quad (15)$$

where  $\alpha$  is a modulation coefficient.

Combined with Equation (12), the internal model controller can be obtained as shown in formula (16):

$$F(s) = \alpha \left( \frac{R_r}{s} + \sigma L_r \right) \quad (16)$$

The controller proposed according to the internal model theory is not difficult from the PI controller in form, but the internal model controller has only one parameter that needs to be adjusted.

If the internal model parameters are completely consistent with the actual system parameters, the actual input signal can be replaced by the internal model's response to the output signal. Giving the definition of the system output estimate  $\hat{Y}(s)$ , which is shown in Equations (17) and (18):

$$\hat{Y}(s) = \begin{bmatrix} \hat{i}_{rd}(s) \\ \hat{i}_{rq}(s) \end{bmatrix} = \frac{1}{R_r + s\sigma L_r} \begin{bmatrix} u_{rd0}(s) \\ u_{rq0}(s) \end{bmatrix} \quad (17)$$

$$\hat{u}_r' = \begin{bmatrix} \hat{u}_{rd}' \\ \hat{u}_{rq}' \end{bmatrix} = \begin{bmatrix} -(\omega_1 - \omega_r)\sigma L_r \hat{i}_{rq} \\ (\omega_1 - \omega_r)\left(\frac{L_m}{L_s}\psi_s + \sigma L_r \hat{i}_{rd}\right) \end{bmatrix} \quad (18)$$

An open-loop internal model controller is obtained, which is shown in Figure 6.

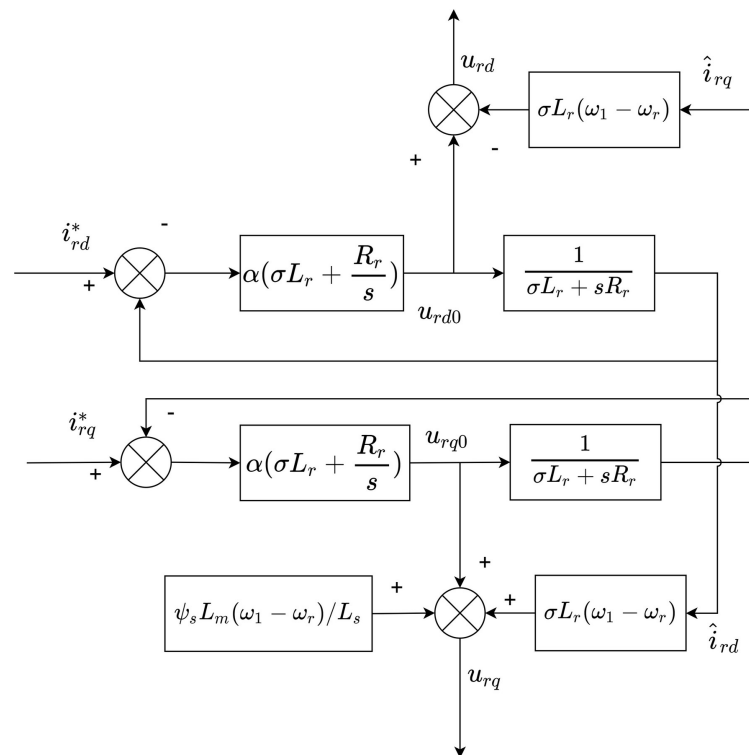


Figure 6. Description of the internal model open-loop controller.

### 3.2. Integral Sliding Mode Compensation

Due to external disturbances in the actual system, the model parameters may not be accurate enough. The estimated current of the open-loop controller will deviate from the actual current. Therefore, in order to improve the robustness of the control system, a sliding mode control strategy is introduced. The tracking error function is defined as shown in Equation (19):

$$\begin{cases} e = \begin{bmatrix} \hat{i}_{rd} \\ \hat{i}_{rq} \end{bmatrix} + z \\ \dot{z} = \frac{R_r}{\sigma L_r} \begin{bmatrix} i_{rd} \\ i_{rq} \end{bmatrix} - \frac{1}{\sigma L_r} \begin{bmatrix} u_{rd} - \hat{u}_{rd}' \\ u_{rq} - \hat{u}_{rq}' \end{bmatrix} \\ z(0) = [0 \ 0]^T \end{cases} \quad (19)$$

The open-loop controller is designed based on the internal model control theory. It can achieve good performance when the system reaches the equilibrium position, but when the system state is unbalanced at the initial moment and there is external interference, the internal-mode open-loop controller cannot obtain good control performance. For such applications, the integral sliding mode theory can be introduced to design the integral sliding mode surface. According to the integral sliding mode theory, the sliding mode surface is usually defined according to Equation (20):

$$S(t) = \left( \delta + \frac{d}{dt} \right)^{r-1} e(t) + k_i \int_0^\infty e(t) dt \quad (20)$$

where  $r$  is the system order,  $\delta$  is a positive real number, and  $k_i$  is a sliding gain. It can be known from Equation (18) that  $r = 1$  and  $\delta = 1$ .

Integral sliding mode control adds an integral part to the basic sliding mode control method to improve the performance of sliding mode control. Sliding mode control is robust to disturbances only in the sliding mode phase, but it is not robust in the arrival phase. Since the integral sliding mode control includes an integral part, a sliding surface can be designed so that the system is in the sliding mode phase at the initial moment. Thus, the entire state trajectory of the system is on the sliding surface [32]. The designed sliding surface is shown in Equation (21):

$$S(t) = e(t) + k_i \int_0^\infty e(t) dt \quad (21)$$

The current estimate satisfies Equation (22):

$$\frac{d}{dt} \begin{bmatrix} \hat{i}_{rd}(t) \\ \hat{i}_{rq}(t) \end{bmatrix} = \frac{1}{\sigma L_r} \begin{bmatrix} u_{rd0}(t) \\ u_{rq0}(t) \end{bmatrix} - \frac{R_r}{\sigma L_r} \begin{bmatrix} \hat{i}_{rd}(t) \\ \hat{i}_{rq}(t) \end{bmatrix} \quad (22)$$

Substituting Equation (22) into Equation (9), the derivative of the sliding mode surface is shown in Equation (23):

$$\dot{S} = \frac{1}{\sigma L_r} \begin{bmatrix} u_{rd0} + \hat{u}_{rd}' - u_{rd} \\ u_{rq0} + \hat{u}_{rq}' - u_{rq} \end{bmatrix} + \frac{R_r}{\sigma L_r} \begin{bmatrix} i_{rd} - \hat{i}_{rd} \\ i_{rq} - \hat{i}_{rq} \end{bmatrix} + k_i e \quad (23)$$

The stability of sliding mode control can usually be judged by Lyapunov function, as shown in Equation (24):

$$V = \frac{1}{2} S^2 \quad (24)$$

In order to ensure that Lyapunov function is negative definite, that is,  $\dot{V} \leq 0$ , the control law is designed as shown in Equation (25):

$$\begin{bmatrix} u_{rd} \\ u_{rq} \end{bmatrix} = \begin{bmatrix} u_{rd0} + \hat{u}_{rd}' \\ u_{rq0} + \hat{u}_{rq}' \end{bmatrix} + R_r \begin{bmatrix} i_{rd} - \hat{i}_{rd} \\ i_{rq} - \hat{i}_{rq} \end{bmatrix} + \sigma L_r [k_i e + \epsilon \text{sign}(S)] \quad (25)$$

Substituting the above Equation (25) into the Lyapunov function Equation (24), Equation (26) can be obtained:

$$\dot{V} = S^T (-\epsilon \text{sign}(S)) \quad (26)$$

Therefore, as long as the constant  $\epsilon > 0$  is satisfied,  $\dot{V} \leq 0$  can be ensured.

Considering the impact of uncertainties and disturbances on the system, the sliding mode surface can be rewritten into the form of Equation (27):

$$\dot{S} = \frac{1}{\sigma L_r} \begin{bmatrix} u_{rd0} + \hat{u}_{rd}' - u_{rd} \\ u_{rq0} + \hat{u}_{rq}' - u_{rq} \end{bmatrix} + \frac{R_r}{\sigma L_r} \begin{bmatrix} i_{rd} - \hat{i}_{rd} \\ i_{rq} - \hat{i}_{rq} \end{bmatrix} + k_i e + \tau_d \quad (27)$$

where  $\tau_d$  is the influence of the uncertainties and disturbances on the sliding surface. Equation (26) can be rewritten as:

$$\dot{V} = S^T(-\epsilon \text{sign}(S) + \tau_d) \quad (28)$$

As long as  $\epsilon > |\tau_d|$  is satisfied,  $\dot{V} \leq 0$  can be ensured. This shows that the proposed control method can ensure stability under disturbances.

**Remark 1.** According to the characteristics of sliding mode control, the state trajectory of the system will be limited to the sliding surface after the system state moves to the sliding surface. However, in practical systems, due to the inertia of the controlled system and the delay of the switching components, the switching frequency of sliding mode control cannot be infinite. This will cause the trajectory of the system state to not stay on the sliding surface, but to traverse back and forth on the boundary of the sliding surface or to perform periodic motion near the equilibrium point. This high-frequency oscillation phenomenon is called chattering. Chattering affects the control accuracy of the system and cause frequent switching of switching components, shortening the component operation cycle and increasing power consumption.

**Remark 2.** For floating offshore wind turbine systems, if chattering occurs in the DFIG drive control system, it may cause speed fluctuations, torque ripples, and current harmonics. If chattering occurs in the voltage or flux observer, it will cause observation noise and reduce system stability. Although sliding mode control has the advantage of good robustness, to some extent, chattering phenomenon hinders its control advantage. Therefore, the suppression of chattering has become the primary issue in practical application research of sliding mode control.

In the sliding mode control system of this study, due to the introduction of integral sliding mode control, the initial state of the system can be located on the sliding surface. Therefore, the design of the approach law should mainly be considered as the suppression of chattering. Based on the above analysis, the control law is shown by Equation (29):

$$\begin{cases} \dot{S}(t) = -\frac{k}{D(S(t))} \tanh(\gamma S(t)) \\ D(S) = \epsilon + (1 - \epsilon)e^{-\eta|S|} \end{cases} \quad (29)$$

where  $0 < \epsilon < 1$ ,  $\eta > 0$ , and  $\gamma > 0$ ,  $\tanh(S)$  is a hyperbolic tangent function, and its expression is shown in Equation (30):

$$\tanh(S) = \frac{e^S - e^{-S}}{e^S + e^{-S}} \quad (30)$$

The relationship between the sliding function and its derivative under different parameter values is shown in Figure 7.

It can be known from Figure 7 that the approaching speed of the system is related to the current value of the sliding function. The larger the value of the sliding function, the faster the approaching speed. When the state of the system is close to the sliding surface, that is, the sliding function approaches 0, and the properties of the law of approximation approximate the hyperbolic tangent function. At this time, the characteristics of the system are basically determined by parameter  $\gamma$ . The hyperbolic tangent function is a continuous odd function. When it is far from the zero point on the positive semi-axis, its function value is approximately 1. When it is close to the zero point, its function value will rapidly decrease to 0. This characteristic allows the approach law to retain the robustness of the sliding mode control while suppressing chattering. When the parameter  $\epsilon$  is close to 1, the characteristic of the law of approximation over the entire state space is similar to the hyperbolic tangent function. That is, when the system state is far from the sliding surface, the approaching speed is approximately constant. When the system state is close to the

sliding surface, the approaching speed is rapidly reduced to 0. When the parameter  $\epsilon$  is close to 0, the approaching speed farther from the sliding surface approximates an exponential relationship with the value of the sliding function. Therefore, the value of  $\epsilon$  affects the characteristics of the approaching law when it is far away from the sliding surface, that is, the reaching phase of sliding mode control. The parameter  $\eta$  affects the transition process of the two characteristics of the system state when it is far away from and close to the sliding surface. When the value of this parameter is larger, the approach speed will converge closer to the sliding surface.

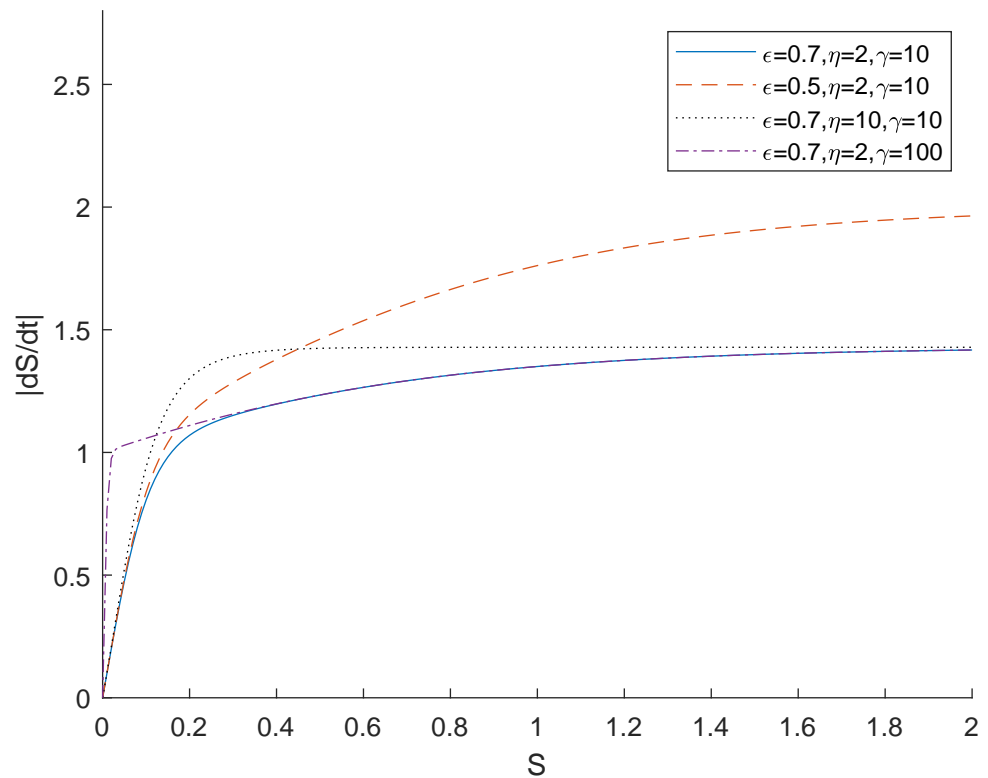


Figure 7. Reaching law under different parameters.

**Theorem 1.** According to the analysis in Equations (29) and (30), the control law of the improved sliding mode controller is shown in Equation (31):

$$\begin{bmatrix} u_{rd} \\ u_{rq} \end{bmatrix} = \begin{bmatrix} u_{rd0} + \hat{u}_{rd}' \\ u_{rq0} + \hat{u}_{rq}' \end{bmatrix} + R_r \begin{bmatrix} i_{rd} - \hat{i}_{rd} \\ i_{rq} - \hat{i}_{rq} \end{bmatrix} + \sigma L_r \left[ k_i e + \frac{k_p}{P(S(t))} \tanh(\gamma S) \right] \quad (31)$$

**Proof.** To verify the stability of the proposed system, substituting the control law (31) into the Lyapunov function described in Equation (24), we can get

$$\dot{V} = -S^T \frac{k}{D(S(t))} \tanh(\gamma S) \quad (32)$$

Since  $0 < \epsilon < 1$ ,  $\eta > 0$ .

$$D(S) = \epsilon + (1 - \epsilon)e^{-\eta|S|} > 0 \quad (33)$$

It can be concluded that

$$\dot{V} = -S^T \frac{k}{D(S(t))} \tanh(\gamma S) \leq 0 \quad (34)$$

The equal sign holds if and only if  $S = 0$ . Therefore, it can be proved that the proposed sliding mode controller meets the stability requirements.  $\square$

Taking the current  $d$ -axis component as an example, the structure of the proposed internal model-integral sliding model controller (IM-ISMC) is shown in Figure 8. As we can see in the figure, in the block diagram of the internal model-integral sliding model controller, an improved approach law has been used on  $u_i$ . Moreover, the tracking error calculation has been used on error  $e$ , and the final output is  $u_{rd}$ .

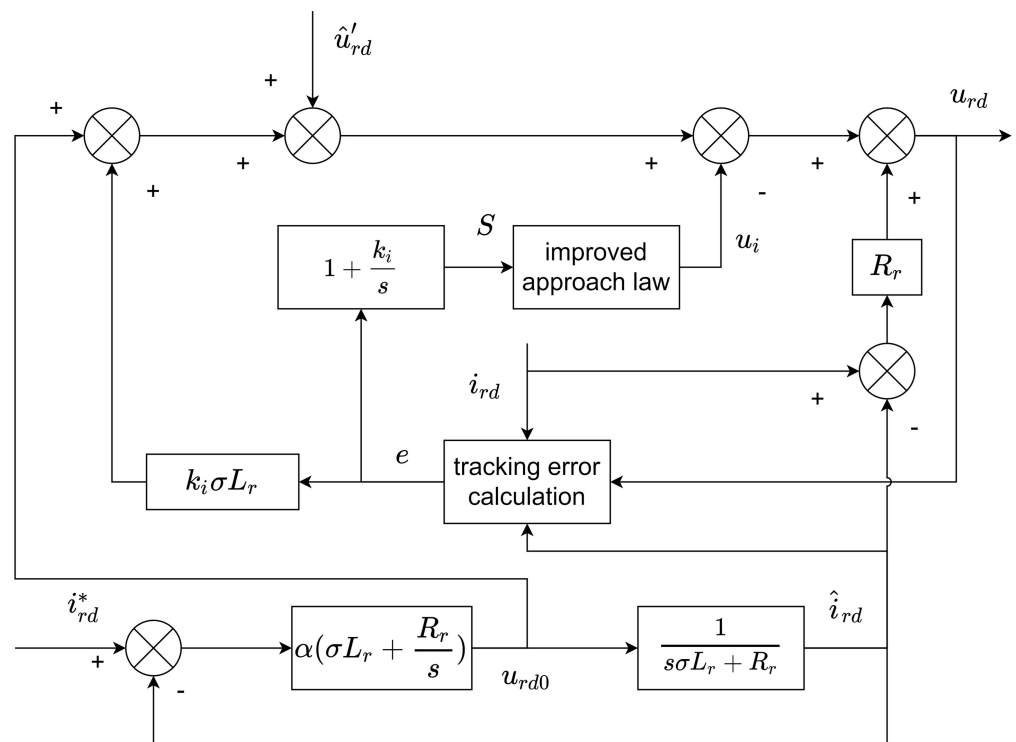


Figure 8. Description of block diagram of the IM-ISMC.

In summary, by using the IM-ISMC controller instead of the PI controller in vector control, an IM-ISMC-based floating offshore wind turbine system can be obtained, as shown in Figure 9. As we can see in the figure, an IM-ISMC controller has been used at the back of PI controller. Moreover, the coordinate transformation has been used on PWM and IGBT, and angle calculation has been used at the back of DFIG.

The proposed control system is based on vector control theory. The relationship between the  $q$ -axis component of the rotor current and the speed can be better described by a linear system, and it can be controlled by a PI controller. The relationship between the  $d$ -axis component of the rotor current and the reactive power is similar. The current is decoupled by the IM-ISMC controller.

The proposed control strategy contains many undetermined parameters, which include modulation coefficient  $\alpha$ , sliding gain  $k_i$ , and related parameters of sliding mode control law  $k_p$ ,  $\epsilon$ ,  $\eta$ , and  $\gamma$ . The Grey Wolf Optimization (GWO) will be used to optimize these parameters.

Grey Wolf Optimization is a meta-heuristic algorithm proposed by Mirjalili of Griffith University [33]. This algorithm is inspired by the hunting behavior and cooperative behavior in the hunting process of gray wolves. The gray wolf family has a strict hierarchical management system. According to leadership, the wolf group can be divided into four levels:  $\alpha$ ,  $\beta$ ,  $\delta$ , and  $\omega$ .

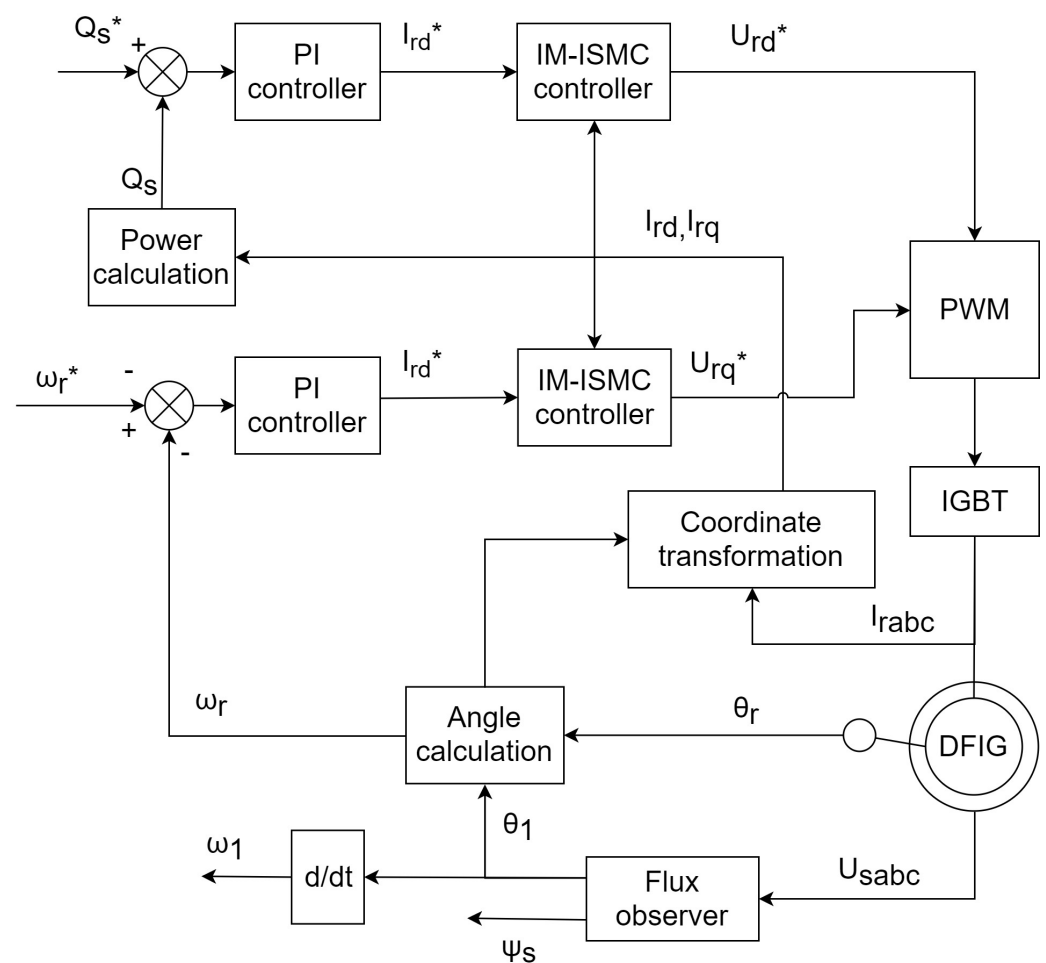


Figure 9. Description of floating offshore wind turbine system based on IM-ISM.

After obtaining the position of the prey, the gray wolves will surround the prey. This process can be expressed by Equation (35):

$$\begin{cases} D_p = |C \cdot X_p(k) - X(k)| \\ X(k+1) = X_p(k) - A \cdot D_p \end{cases} \quad (35)$$

Among them,  $k$  is the number of iterations,  $X(k)$  is the position vector of the gray wolf after performing the  $k$ th iteration,  $X_p(k)$  is the position vector of the prey after performing the  $k$ th iteration,  $A$  and  $C$  are coefficient vectors, and the expressions are shown in Equation (36):

$$\begin{cases} A = 2ar_1 - a \\ C = 2r_2 \end{cases} \quad (36)$$

Among them,  $r_1$  and  $r_2$  are random numbers in the range of  $[0,1]$ .  $a$  is a variable that linearly decreases with the number of iterations, and its value gradually decreases from 2 to 0.

Through the above iterative process, the individual can be redirected to any position around the prey. However, this is not enough to reflect the group wisdom in the gray wolves. When gray wolves are hunting prey, the higher-level gray wolves play a key role in this process. After the encirclement process is completed, the gray wolves will hunt under

the leadership of wolves with three levels of  $\alpha$ ,  $\beta$ , and  $\delta$ . This process can be described by the following equations:

$$\begin{cases} D_\alpha = |C_1 \cdot X_\alpha(k) - X(k)| \\ D_\beta = |C_2 \cdot X_\beta(k) - X(k)| \\ D_\delta = |C_3 \cdot X_\delta(k) - X(k)| \end{cases} \quad (37)$$

$$\begin{cases} X_1 = X_\alpha(k) - A_1 D_\alpha \\ X_2 = X_\beta(k) - A_2 D_\beta \\ X_3 = X_\delta(k) - A_3 D_\delta \end{cases} \quad (38)$$

$$X(k+1) = \frac{X_1 + X_2 + X_3}{3} \quad (39)$$

When the process of encirclement and hunting has been completed by the gray wolves, they will attack the prey. This stage is manifested as the convergence of the solution in the process of solving the optimization problem.

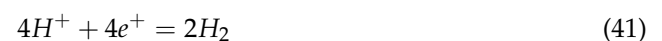
In the offshore wind power generation system proposed in this paper, a set of parameters satisfying the definition are regarded as feasible solutions, and all combinations of parameters satisfying the definition constitute the solution space of the optimization problem. Using the gray wolf optimization algorithm to search in the solution space, the sub-optimal solution can be obtained in a limited time.

Usually, the basic method of power to gas from floating offshore wind power is using electrolysis of sea water to produce hydrogen. The principle of electrolyzing water to produce hydrogen is shown in Figure 10. It can be seen from the figure that the loss of electrons at the anode produces oxygen, and the electrons at the cathode produce hydrogen. The solution mixed in water increases the conductivity of the electrolyte. That is to say, the electrolysis of water is to immerse the cathode and anode in the electrolytic cell in water and apply direct current, respectively. The water will be decomposed and produce hydrogen at the cathode and oxygen at the anode. The main chemical reaction equations of the electrode reaction are as follows:

In the water,



The point of cathode,



The point of anode,



The chemical equation for the overall reaction is:



The industrial experiment intends is to use a megawatt-class floating offshore wind turbine and hydrogen production equipment to verify the optimization effect of the control system. From the perspective of the system, concrete floating foundation, offshore wind turbine, hydrogen production equipment, the theory, method, and algorithm of this research can be verified step by step. At the same time, during the verification process, the floating offshore wind power sensing device is used to obtain the real-time status information of the intelligent control operation energy conversion online, and the controller data acquisition device is used to obtain the status information related to the wind power operation and the hydrogen production process. All relevant data are collected and aggregated through the distributed information network system. The non-grid-connected hydrogen production and logistics of floating offshore wind power to be used in industrial experiments are shown in Figure 11.

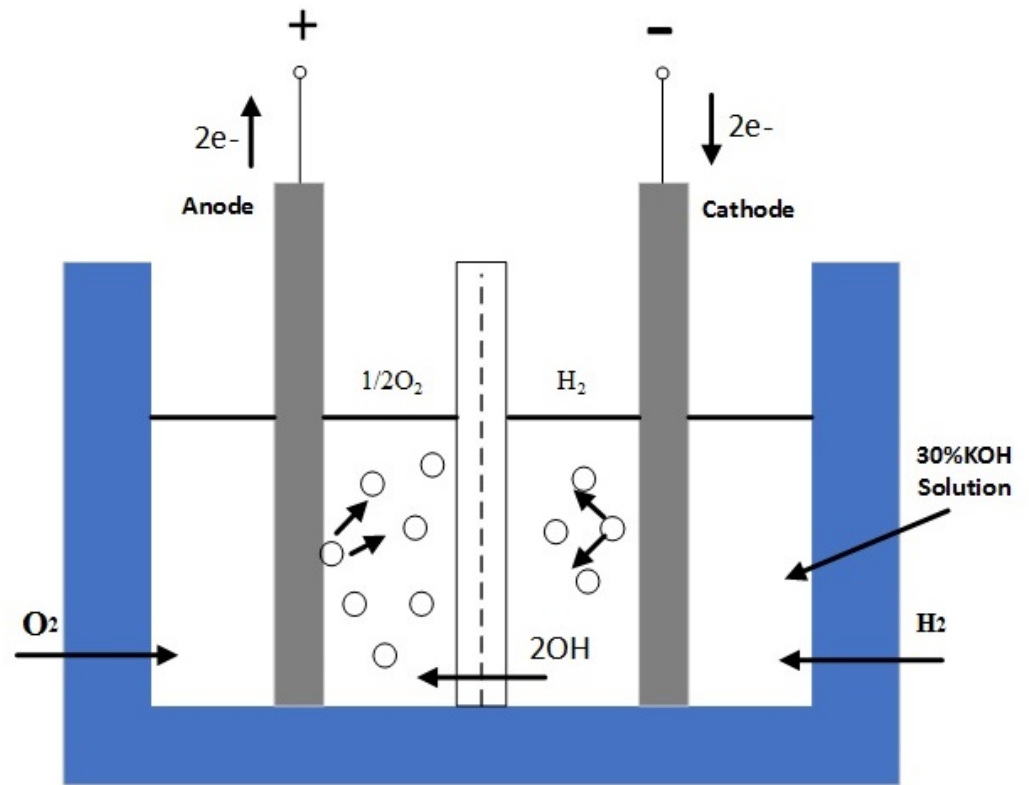


Figure 10. The principle of hydrogen production by water electrolysis of floating offshore wind power.

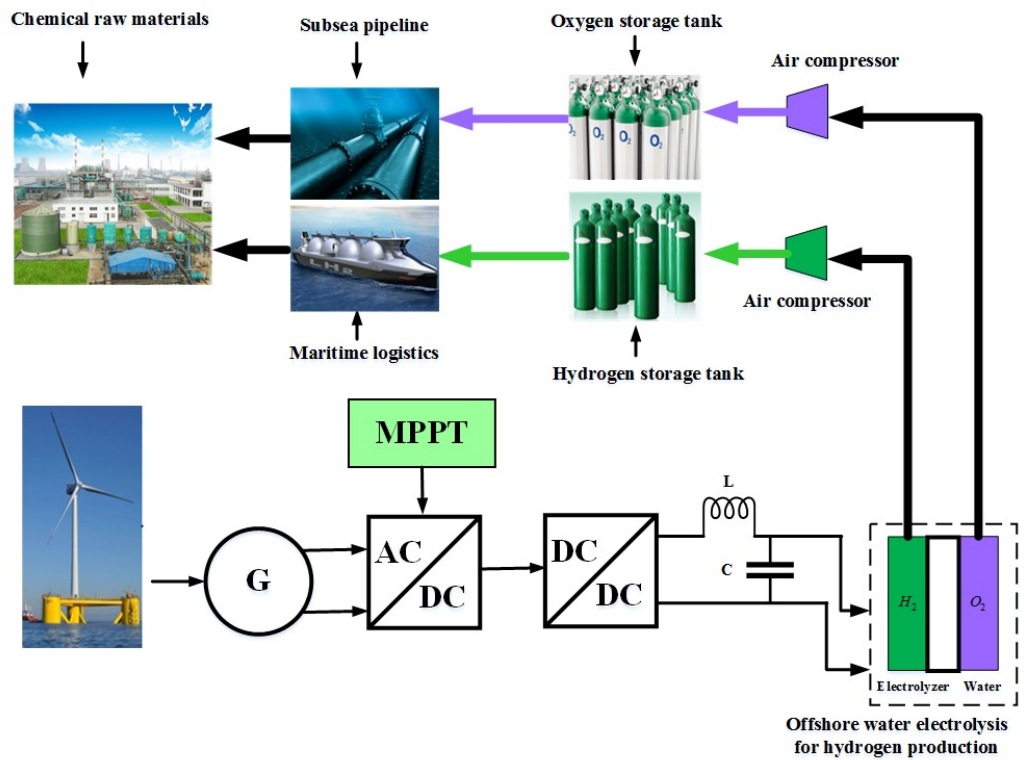


Figure 11. The description of the non-grid-connected hydrogen production and logistics of floating offshore wind power.

#### 4. Simulation Results

To verify the effectiveness of the proposed controller, MATLAB/Simulink is used for simulation verification. The DFIG parameters used in the simulation are shown in Table 1. The values of the parameters in the table are selected with reference to real 2 MW wind turbines.

**Table 1.** DFIG parameters.

Name	Value	Unit
Rated power	2000	kW
Stator voltage	690	V
Number of pole pairs (p)	2	
Voltage frequency	50	Hz
Stator resistance ( $R_s$ )	0.0025	ohm
Rotor resistance ( $R_r$ )	0.003	ohm
Mutual inductance ( $L_m$ )	2.5	mH
Stator inductance ( $L_s$ )	2.51	mH
Rotor inductance ( $L_r$ )	2.51	mH
Moment of inertia (J)	120	kg·m <sup>2</sup>

The effect of the controller is evaluated by testing the response of the control system at random wind speeds. Considering that the maximum point tracking operation of the floating offshore wind turbine is between the cut-in wind speed and the rated wind speed, the wind speeds used in the simulation are in the interval from 3 m/s to 12 m/s. It is shown in Figure 12.

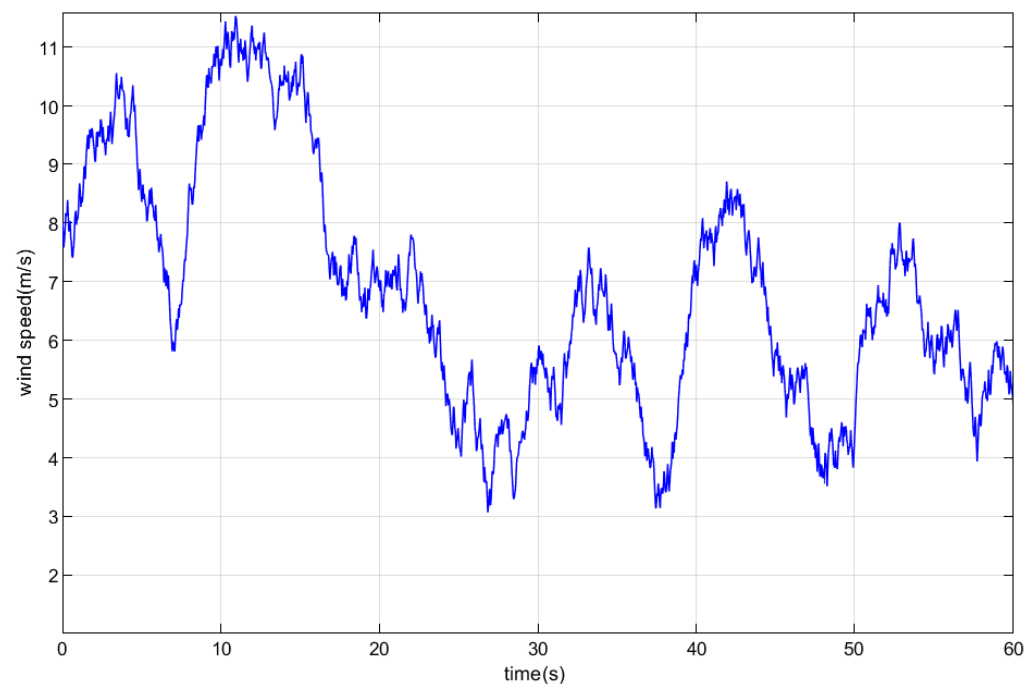


**Figure 12.** Wind speed characteristics.

Figure 13 shows the variation curve of the rotor speed when the proposed controller and PI controller are used. Figures 14–16 are the rotor speed in the intervals of 3 s, 7 s, 7 s, 11 s, and 11 s, 15 s, which are obtained by magnifying the three parts of Figure 13. Due to the mechanical inertia of the generator, there is a certain delay between the actual speed and the reference speed. Overall, the proposed controller has better dynamic response speed than the PI controller.

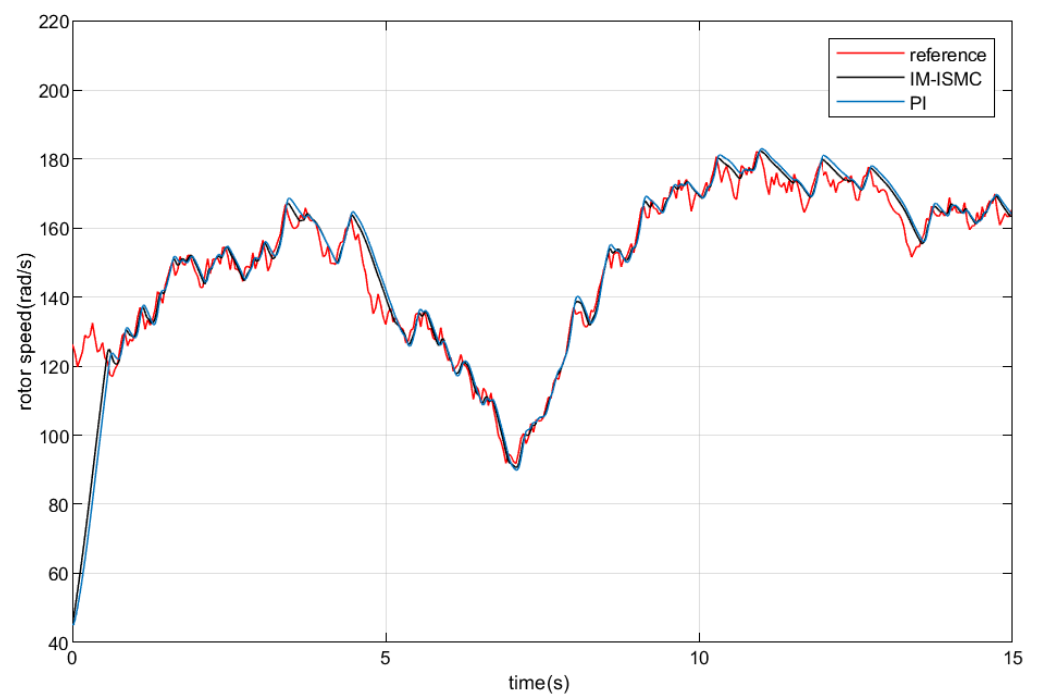


Figure 13. Simulation results of rotor speed.

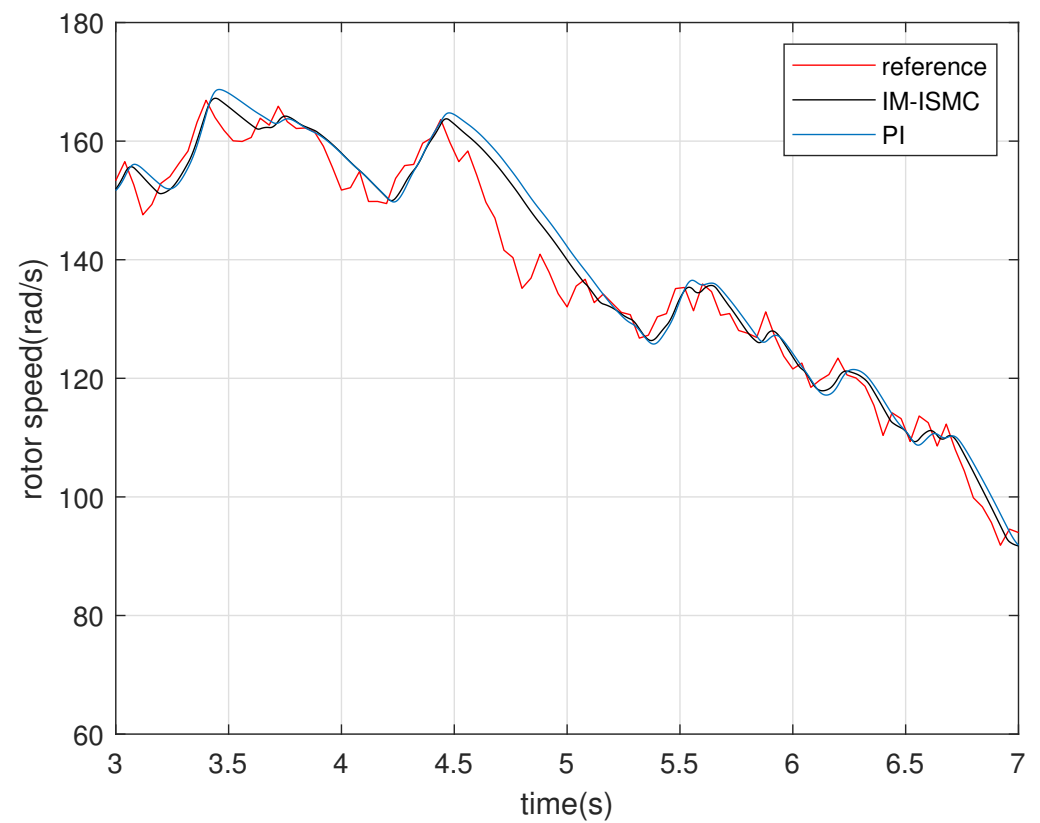


Figure 14. Rotor speed 3–7 s enlarged view.

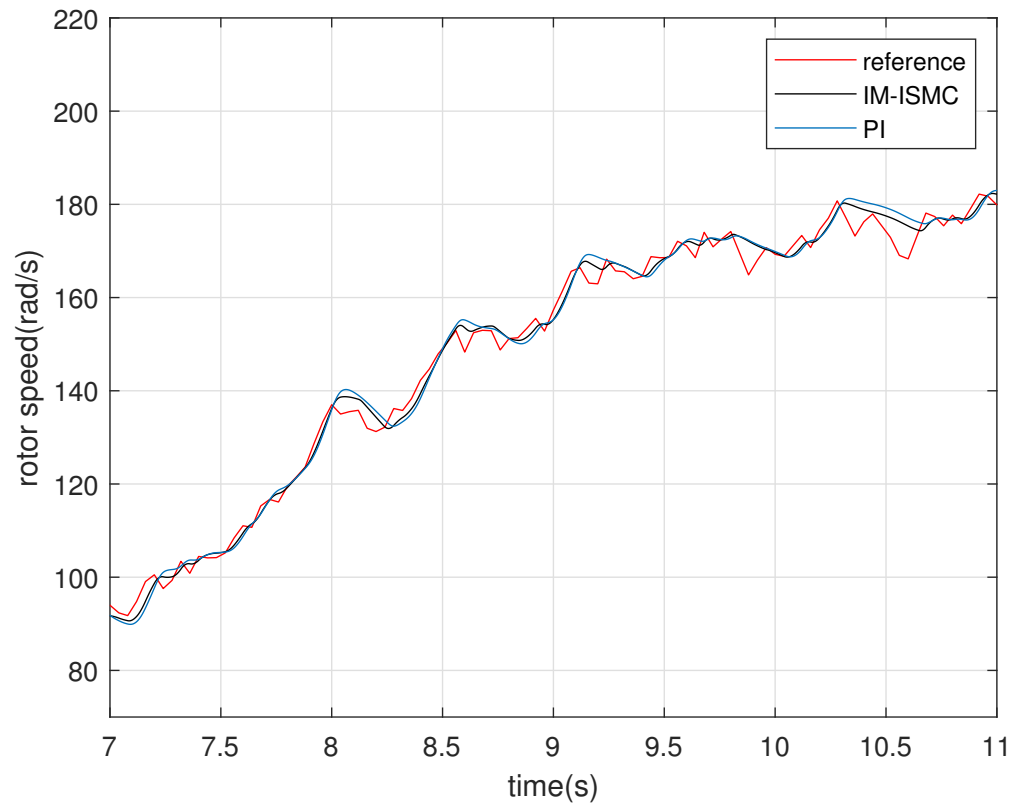


Figure 15. Rotor speed 7–11 s enlarged view.

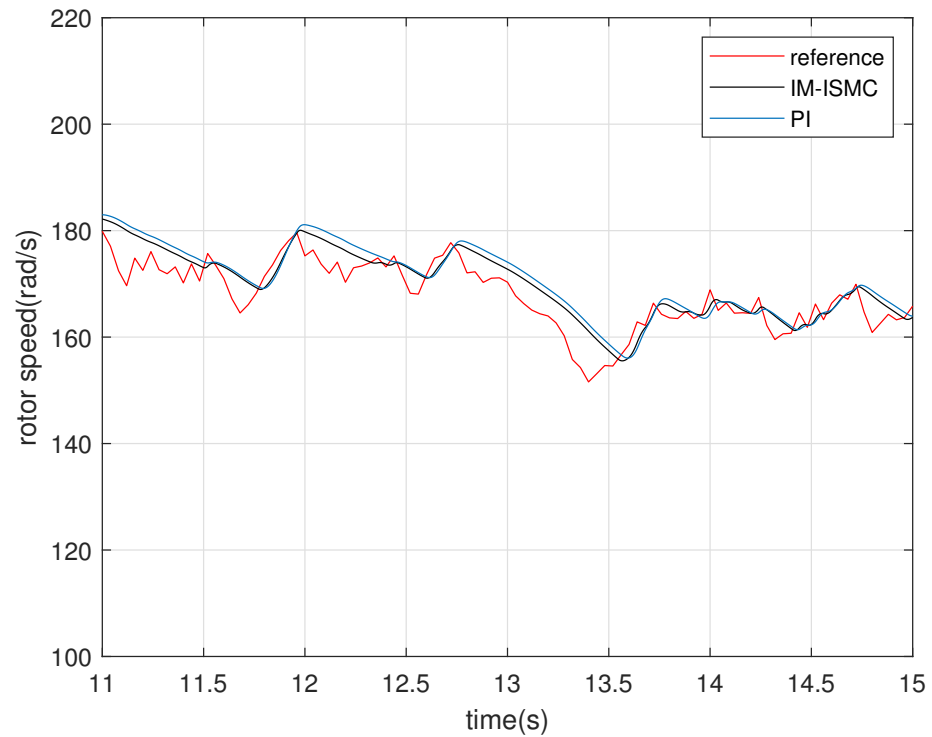
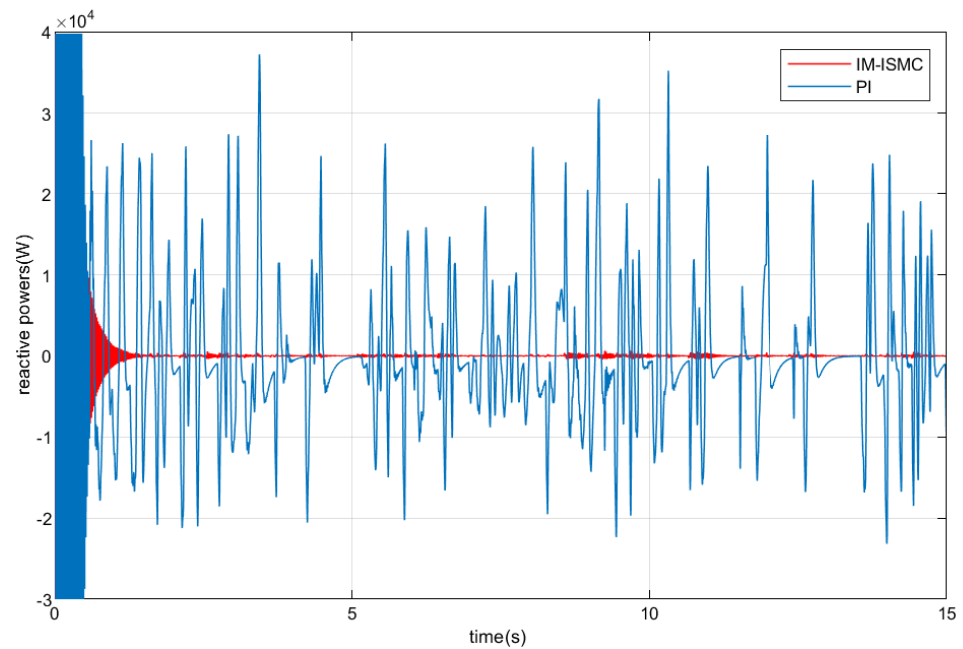


Figure 16. Rotor speed 11–15 s enlarged view.

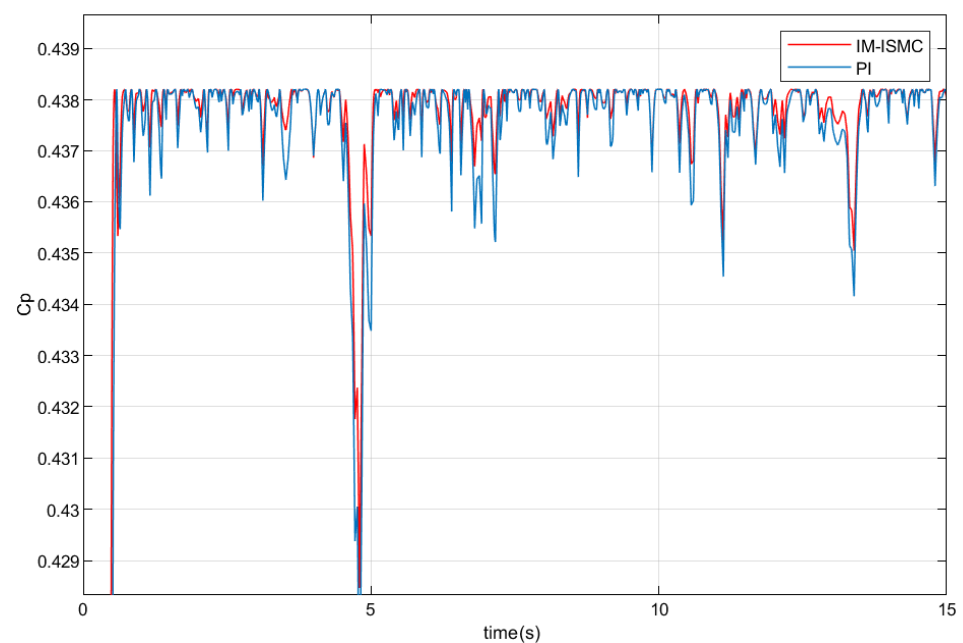
Figure 17 shows the corresponding reactive power curves of the two controllers. The reference value of reactive power is 0 W. The proposed controller can converge faster,

but the PI controller will oscillate near the equilibrium position. Therefore, the proposed controller has better steady-state performance than the PI controller.



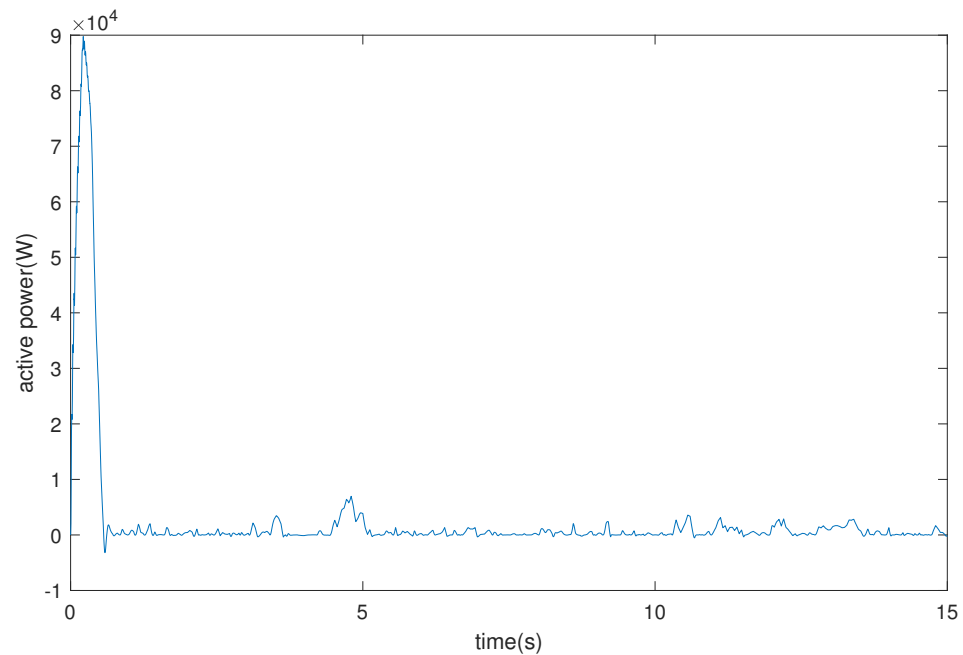
**Figure 17.** Simulation results of reactive power.

Figure 18 shows the simulation results of the power coefficient. The maximum power coefficient is 0.438 approximately. The proposed controller can adjust the rotor speed according to the change of wind speed, so the power coefficient of IM-ISM controller is larger than PI controller in general. The purpose of the maximum power point tracking is to capture wind energy as much as possible, and the offshore wind energy power coefficient can be used as the basis for determining the amount of captured offshore wind energy. This means that floating offshore wind turbine systems can capture more offshore wind energy by using the proposed controller.



**Figure 18.** Simulation results of power coefficient.

Figure 19 shows the different active power between the PI controller and the proposed controller. They are obtained by subtracting the active power value of the PI controller from the active power value of the proposed controller. At the beginning of the simulation, the power differential reaches its maximum value of 90 kW or so. In general, the proposed controller has higher active power than a PI controller at all times, especially in the time of the rotor increasing speed.



**Figure 19.** The active power between the PI controller and the proposed controller.

## 5. Conclusions

A current decoupling controller is presented for DFIG wind power systems on a floating offshore wind turbine to achieve MPPT. By using the internal model control strategy, an internal model open-loop controller is designed to simplify the parameter design. Moreover, the sliding mode control theory is used to achieve dynamic compensation based on the internal model open-loop controller, whereas the integral sliding mode controller is used to compensate the output error of the open-loop controller, and the parameters of proposed controller are designed through Gray Wolf Optimization. In addition, the performance of the controller is verified by testing the response of the controller under random wind speed in simulation software. Simulation results show that the proposed controller is superior to traditional PI controllers in terms of dynamic response and steady-state error. However, the proposed controller is not implemented on real floating offshore wind turbines. At the same time, how the controller parameters affect the control results has not been studied in depth. In future research, it is possible to build an experimental platform to conduct further research on the field of hydrogen production by floating offshore wind power.

**Author Contributions:** L.P.: Conceptualization, Methodology, Software, Data curation, Supervision, Writing—review & editing, Formal analysis, Resources; Z.Z.: Conceptualization, Visualization, Investigation, Software, Validation, Funding acquisition, Project administration; Y.X.: Writing—review & editing, Formal analysis, Resources, Software; J.S.: Visualization, Investigation, Software, Validation, Writing—original draft. All authors have read and agreed to the published version of the manuscript.

**Funding:** This work was supported by the Foundation of Zhongshan Institute of Advanced Engineering Technology of WUT (Grant No. WUT202001), China. This work was also supported by projects from Key Lab. of Marine Power Engineering and Tech. authorized by MOT (KLMPET2020-01), the

Fundamental Research Funds for the General Universities (WUT: 2021III007GX) and Shaoxing City Program for Talents Introduction, China.

**Institutional Review Board Statement:** Not applicable.

**Informed Consent Statement:** Not applicable.

**Data Availability Statement:** The study did not report any data.

**Acknowledgments:** This work was supported by the Foundation of Zhongshan Institute of Advanced Engineering Technology of WUT (Grant No. WUT202001), China. This work was also supported by projects from the Key Lab of Marine Power Engineering and Tech authorized by MOT (KLMPET2020-01), the Fundamental Research Funds for the General Universities (WUT: 2021III007GX), and Shaoxing City Program for Talents Introduction, China.

**Conflicts of Interest:** The authors declare no conflict of interest.

## References

- Chatzinikolaou, S.D.; Oikonomou, S.D.; Ventikos, N.P. Health externalities of ship air pollution at port-Piraeus port case study. *Transp. Res. Part Transp. Environ.* **2015**, *40*, 155–165. [\[CrossRef\]](#)
- Pfeifer, A.; Krajačić, G.; Ljubas, D.; Duić, N. Increasing the integration of solar photovoltaics in energy mix on the road to low emissions energy system-Economic and environmental implications. *Renew. Energy* **2019**, *143*, 1310–1317. [\[CrossRef\]](#)
- Cardenas, R.; Peña, R.; Alepuz, S.; Asher, G. Overview of control systems for the operation of DFIGs in wind energy applications. *IEEE Trans. Ind. Electron.* **2013**, *60*, 2776–2798. [\[CrossRef\]](#)
- Akhbari, A.; Rahimi, M. Control and stability analysis of DFIG wind system at the load following mode in a DC microgrid comprising wind and microturbine sources and constant power loads. *Int. J. Electr. Power Energy Syst.* **2020**, *117*, 105622. [\[CrossRef\]](#)
- Kadri, A.; Marzougui, H.; Aouiti, A.; Bacha, F. Energy management and control strategy for a DFIG wind turbine/fuel cell hybrid system with super capacitor storage system. *Energy* **2020**, *192*, 116518. [\[CrossRef\]](#)
- Xiahou, K.; Liu, Y.; Li, M.; Wu, Q. Sensor fault-tolerant control of DFIG based wind energy conversion systems. *Int. J. Electr. Power Energy Syst.* **2020**, *117*, 105563. [\[CrossRef\]](#)
- Lu, K.; Zhou, W.; Zeng, G.; Zheng, Y. Constrained population extremal optimization-based robust load frequency control of multi-area interconnected power system. *Int. J. Electr. Power Energy Syst.* **2019**, *105*, 249–271. [\[CrossRef\]](#)
- Zeng, G.Q.; Xie, X.Q.; Chen, M.R.; Weng, J. Adaptive population extremal optimization-based PID neural network for multivariable nonlinear control systems. *Swarm Evol. Comput.* **2019**, *44*, 320–334. [\[CrossRef\]](#)
- Zhang, C.; Zhang, Y.; Shi, X.; Alpanidis, G.; Fan, G.; Shen, X. On Incremental Learning for Gradient Boosting Decision Trees. *Neural Process. Lett.* **2019**, *50*, 957–987. [\[CrossRef\]](#)
- Pan, L.; Wang, X. Variable pitch control on direct-driven PMSG for offshore wind turbine using Repetitive-TS fuzzy PID control. *Renew. Energy* **2020**, *159*, 221–237. [\[CrossRef\]](#)
- Qi, Y.; Liu, Y.; Fu, J.; Zeng, P. Event-triggered  $L_\infty$  control for network-based switched linear systems with transmission delay. *Syst. Control. Lett.* **2019**, *134*, 104533. [\[CrossRef\]](#)
- Qi, Y.; Liu, Y.; Niu, B. Event-Triggered  $H_\infty$  Filtering for Networked Switched Systems With Packet Disorders. *IEEE Trans. Syst. Man Cybern.* **2019**, *51*, 2847–2859. [\[CrossRef\]](#)
- Hamed, Y.S.; Aly, A.A.; Saleh, B.; Alogla, A.F.; Alharthi, M.M. Nonlinear Structural Control Analysis of an Offshore Wind Turbine Tower System. *Processes* **2020**, *8*, 22. [\[CrossRef\]](#)
- Chen, Z.; Wang, X.; Kang, S. Effect of the Coupled Pitch–CYaw Motion on the Unsteady Aerodynamic Performance and Structural Response of a Floating Offshore Wind Turbine. *Processes* **2021**, *9*, 290. [\[CrossRef\]](#)
- Mozayan, S.M.; Saad, M.; Vahedi, H.; Fortin-Blanchette, H.; Soltani, M. Sliding mode control of PMSG wind turbine based on enhanced exponential reaching law. *IEEE Trans. Ind. Electron.* **2016**, *63*, 6148–6159. [\[CrossRef\]](#)
- Bossoufi, B.; Karim, M.; Lagrioui, A.; Taoussi, M.; Derouich, A. Observer backstepping control of DFIG-Generators for wind turbines variable-speed: FPGA-based implementation. *Renew. Energy* **2015**, *81*, 903–917. [\[CrossRef\]](#)
- Yang, B.; Yu, T.; Shu, H.; Dong, J.; Jiang, L. Robust sliding-mode control of wind energy conversion systems for optimal power extraction via nonlinear perturbation observers. *Appl. Energy* **2018**, *210*, 711–723. [\[CrossRef\]](#)
- Kazmi, S.M.R.; Goto, H.; Guo, H.J.; Ichinokura, O. A novel algorithm for fast and efficient speed-sensorless maximum power point tracking in wind energy conversion systems. *IEEE Trans. Ind. Electron.* **2010**, *58*, 29–36. [\[CrossRef\]](#)
- Pan, L.; Shao, C. Wind energy conversion systems analysis of PMSG on offshore wind turbine using improved SMC and Extended State Observer. *Renew. Energy* **2020**, *161*, 149–161. [\[CrossRef\]](#)
- Li, M.; Xiao, H.; Pan, L.; Xu, C. Study of Generalized Interaction Wake Models Systems with ELM Variation for Off-Shore Wind Farms. *Energies* **2019**, *12*, 863. [\[CrossRef\]](#)
- Colombo, L.; Corradini, M.; Ippoliti, G.; Orlando, G. Pitch angle control of a wind turbine operating above the rated wind speed: A sliding mode control approach. *ISA Trans.* **2020**, *96*, 95–102. [\[CrossRef\]](#)

22. Laina, R.; Lamzouri, F.E.Z.; Boufounas, E.M.; El Amrani, A.; Boumhidi, I. Intelligent control of a DFIG wind turbine using a PSO evolutionary algorithm. *Procedia Comput. Sci.* **2018**, *127*, 471–480. [[CrossRef](#)]
23. Youness, E.M.; Aziz, D.; Abdelaziz, E.G.; Jamal, B.; Najib, E.O.; Othmane, Z.; Khalid, M.; Bossoufi, B. Implementation and validation of backstepping control for PMSG wind turbine using dSPACE controller board. *Energy Rep.* **2019**, *5*, 807–821. [[CrossRef](#)]
24. Xiong, L.; Li, P.; Wang, J. High-order sliding mode control of DFIG under unbalanced grid voltage conditions. *Int. J. Electr. Power Energy Syst.* **2020**, *117*, 105608. [[CrossRef](#)]
25. Abolvafaei, M.; Ganjefar, S. Maximum power extraction from wind energy system using homotopy singular perturbation and fast terminal sliding mode method. *Renew. Energy* **2020**, *148*, 611–626. [[CrossRef](#)]
26. Mbukani, M.W.K.; Gule, N. Evaluation of an STSMO-based estimator for power control of rotor-tied DFIG systems. *IET Electr. Power Appl.* **2019**, *13*, 1871–1882. [[CrossRef](#)]
27. Han, Y.; Ma, R. Adaptive-Gain Second-Order Sliding Mode Direct Power Control for Wind-Turbine-Driven DFIG under Balanced and Unbalanced Grid Voltage. *Energies* **2019**, *12*, 3886. [[CrossRef](#)]
28. Nguyen, T.T. A Rotor-Sync Signal-Based Control System of a Doubly-Fed Induction Generator in the Shaft Generation of a Ship. *Processes* **2019**, *7*, 188. [[CrossRef](#)]
29. Asghar, A.B.; Liu, X. Estimation of wind turbine power coefficient by adaptive neuro-fuzzy methodology. *Neurocomputing* **2017**, *238*, 227–233. [[CrossRef](#)]
30. Dai, J.; Liu, D.; Wen, L.; Long, X. Research on power coefficient of wind turbines based on SCADA data. *Renew. Energy* **2016**, *86*, 206–215. [[CrossRef](#)]
31. Mohammadi, E.; Fadaeinedjad, R.; Moschopoulos, G. Implementation of internal model based control and individual pitch control to reduce fatigue loads and tower vibrations in wind turbines. *J. Sound Vib.* **2018**, *421*, 132–152. [[CrossRef](#)]
32. Nayeh, R.F.; Moradi, H.; Vossoughi, G. Multivariable robust control of a horizontal wind turbine under various operating modes and uncertainties: A comparison on sliding mode and  $H_\infty$  control. *Int. J. Electr. Power Energy Syst.* **2020**, *115*, 105474. [[CrossRef](#)]
33. Mirjalili, S.; Mirjalili, S.M.; Lewis, A. Grey wolf optimizer. *Adv. Eng. Softw.* **2014**, *69*, 46–61. [[CrossRef](#)]